Research Square

Preprints are preliminary reports that have not undergone peer review.
They should not be considered conclusive, used to inform clinical practice,
or referenced by the media as validated information.

In situ measurement of non-thermal ion acceleration in collisional laboratory magnetic reconnection

Lee Suttle

ls910@imperial.ac.uk

Imperial College London https://orcid.org/0000-0001-8777-0291

Jonathan Halliday

STFC Rutherford Appleton Laboratory https://orcid.org/0000-0003-1842-9393

Samuel Totorica

Princeton University

Frederico Fiuza

Instituto Superior Tecnico, University of Lisbon https://orcid.org/0000-0002-8502-5535

Aidan Crilly

Imperial College https://orcid.org/0000-0002-0429-9332

Vicente Valenzuela-Villaseca

Lawrence Livermore National Laboratory

Colin Bruulsema

Lawrence Livermore National Laboratory

Wojciech Rozmus

University of Alberta

Stefano Merlini

Imperial College London

Jack Hare

Cornell University

Sergey Lebedev

Imperial College https://orcid.org/0000-0002-9858-8468

Article

Keywords:

Posted Date: November 20th, 2026

DOI: https://doi.org/10.21203/rs.3.rs-10668007/v1

License: This work is licensed under a Creative Commons Attribution 4.0 International License.
Read Full License

Additional Declarations: There is **NO** Competing Interest.

In situ measurement of non-thermal ion acceleration in collisional laboratory magnetic reconnection

L.G. Suttle[1], J.W.D. Halliday[2], S.R. Totorica[3], F. Fiuza[4], A.J. Crilly[1], V. Valenzuela-Villaseca[5,6], C. Bruulsema[5], W. Rozmus[7], S. Merlini[1], J.D. Hare[8], S.V. Lebedev[1]

[1]Blackett Laboratory, Imperial College London, SW7 2BW, United Kingdom
[2]STFC Rutherford Appleton Laboratory, Didcot, OX11 0QX, United Kingdom
[3]Department of Astrophysical Sciences, Princeton University, NJ 08544, USA
[4]GAP/Instituto de Plasmas e Fusão Nuclear, Instituto Superior Técnico, Universidade de Lisboa, Portugal
[5]Lawrence Livermore National Laboratory, Livermore, CA 94550, USA
[6]Plasma Science and Fusion Center, Massachusetts Institute of Technology, Cambridge, MA 02139, USA
[7]Department of Physics, University of Alberta, Edmonton T6G 2E1, Alberta, Canada
[8]Laboratory of Plasma Studies, Cornell University, Ithaca, NY 14853, USA

ABSTRACT (200/200 words)

Magnetic reconnection is an inherent ingredient in plasmas – through space and astrophysics, to the pursuit of controlled nuclear fusion. Reconnection results in the explosive release of stored magnetic energy and may drive some of the most powerful particle acceleration events in the Universe. Despite decades of theoretical, laboratory and observational studies, the mechanisms and conditions under which reconnection can accelerate particles to non-thermal energies remains strongly debated. Here we present the first in situ laboratory measurements of non-thermal ion acceleration in collisional reconnection. Our setup drives magnetized plasma flows into a reconnection layer probed using optical Thomson scattering. We observe a 6σ enhancement in scattered power parallel to the reconnecting electric field, with a spectral shape inconsistent with ion-acoustic turbulent enhanced scattering. Employing Markov Chain Monte Carlo and Automatic Differentiation to fit the scattered spectrum without classic, thermal assumptions, we discover an anisotropic, non-thermal tail in the ion distribution that is corroborated by fully-kinetic simulations of our system. These results demonstrate non-thermal particle acceleration in a regime where frequent particle collisions have long been expected to preclude such a departure from equilibrium, and therefore indicate reconnection can be a non-thermal driver under conditions far more widespread than previously thought possible.

MAIN TEXT (3072/3000 words)

Introduction (437 words)

Magnetic reconnection is a fundamental phenomenon in plasmas, where oppositely directed magnetic field lines break and restructure to energetically favorable configurations[1]. Reconnection occurs widely across vastly different systems and scales: from nuclear fusion devices[2–4], to driving spectacular aurorae in the Earth's magnetosphere[5], and is central to extreme astrophysical events such as Solar[6] and black hole flares[7,8]. Its action provides a rapid release of stored magnetic energy to accelerate particles, and could be attributed to some of the highest energy cosmic ray signatures observed in our universe[9–11].

The mechanisms responsible for reconnection under different physical conditions are diverse and understanding their potential to cause significant changes in energy partition and drive particle

distributions away from thermal equilibrium has long been a scientific challenge[12–14]. Numerous theoretical and computational studies indicate reconnection provides an efficient means of accelerating particles to non-thermal energies, particularly in collisionless[15–17] and relativistic regimes[18–21]. Space probes have a long history of making in situ observations of particle distributions with non-thermal characteristics in our Solar system[22–25], but inferring their sources and connection to the global topology of their reconnecting systems is challenging[26]. Meanwhile, in laboratory reconnection, where global scales can be observed simultaneously with local measurements, direct evidence of non-thermal particles is limited. Recent experiments in collisionless electron-only[27] and magnetically-dominated[28] regimes showed signatures of non-thermal electron acceleration, but until now, no conclusive measurements of non-thermal ion acceleration have been made.

Here, we present the first measurements of a non-thermal, tailed ion distribution from laboratory reconnection, which occurs in a collisional regime at low Lundquist number and non-relativistic conditions. Our experiments were carried out using a platform of electrically pulsed wire arrays, driving counter-propagating magnetized plasma flows to produce a well-defined and dynamically-stable reconnection layer. This layer was probed using optical Thomson scattering (OTS), which allowed us to observe the spectra of ion-acoustic waves (IAWs) in the reconnecting plasma. This technique is established in the field of High-Energy-Density physics for making local measurements of plasma temperatures and velocities by fitting the form of the OTS spectra[29]. Here, we made a novel extension by additionally examining the scattered power from IAWs to detect departures in the ion distribution function from thermal equilibrium. Our Bayesian inference analysis of the spectra allowed us to quantify the shape of the non-thermal distribution out to many times the ion thermal velocity. This counter-intuitive result is corroborated by fully-kinetic simulations, and suggests direct pumping of ions by the reconnection electric field, indicating non-thermal ion acceleration can occur even in collisional plasmas and therefore play an important role in dictating the energy partition of a wide range of systems.

Laboratory reconnection in super-Alfvénic, collisional flows (446 words)

Our experiments were conducted at the MAGPIE pulsed-power laboratory[30] using the setup depicted in Fig. 1. This consisted of two radially expanding plasma flows, produced by cylindrical wire arrays ablated by a 1 MA-peak current pulse[31]. The flows were driven by the $\boldsymbol{J} \times \boldsymbol{B}$ force, sustained over the 500 ns duration of the applied current. The current embeds azimuthal magnetic fields into the flows[31], which collide with anti-parallel *B*-vectors. This forms a reconnection layer (current sheet) with magnetic field restructuring in the reconnection (*xy*) plane.

This platform has previously used either aluminum or carbon plasmas, producing reconnection under contrasting conditions[32]. Here we employed aluminum plasmas, producing a reconnection layer with Lundquist number $S = LV_A/\eta \sim 20$ (where *L* is the layer length, V_A the inflow Alfvén velocity and η the plasma resistivity). Notably, the reconnection is collisional, with half-thickness $\delta \approx$ the ion skin depth d_i, where both scales greatly exceed the ion-ion mean free path λ_{ii} ($d_i/\lambda_{ii} \sim 10^4$). Additionally, the inflow velocity is supersonic and super-Alfvénic ($M_s = 3, M_A = 1.5$), placing the system in the flow-

dominated magnetohydrodynamic regime. Here, the inflowing electrons are moderately magnetized (Hall parameter $\Omega_{ce}\tau_{ei}\sim 1$), while the ions are unmagnetized ($\Omega_{ci}\tau_{ii}\sim 0.001$). Nevertheless, magnetic energy released by reconnection plays an important role in the system energy balance[33,34].

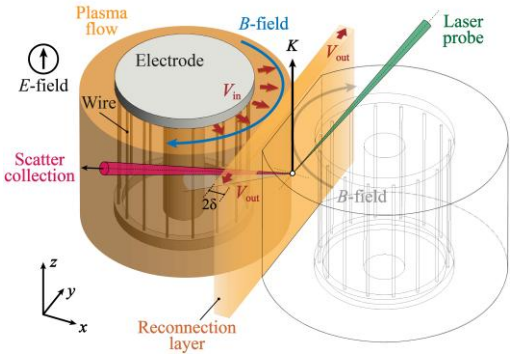


Fig. 1 | Experimental setup and Thomson scattering geometry. The reconnection layer was produced by the collision of two radially expanding, magnetized plasma flows. The flows were generated by the ablation of two cylindrical arrays of aluminum wires by an applied current pulse (one inflow and wire array are shown transparent here for clarity). The current pulse was split in parallel between the wire arrays, giving rise to oppositely-directed magnetic fields advected by the flows. The plasma in both the inflow regions and reconnection layer was probed using a focusing laser beam. Thomson scattered light was collected in the direction (with respect to the probe) that yielded a resultant wavevector $\boldsymbol{K}$, aligned with the out-of-plane axis – parallel to the reconnection electric field $\boldsymbol{E_{rec}} \parallel \boldsymbol{V_{in}} \times \boldsymbol{B_y}$. The observed TS spectra were thus sensitive to plasma motion in this direction.

Inside the reconnection layer the kinetic and magnetic energy from the inflows is converted to kinetic and thermal energy in the plasma. Extensive characterization of this was provided in past work[33,34] using interferometry, Faraday rotation polarimetry and OTS diagnostics[35,36]. The OTS measurements were sensitive only to components of motion in the reconnection plane (perpendicular to the reconnection electric field $\boldsymbol{E_{rec}}$). They showed a heating of the plasma inside the layer, accompanied by fast exhausts in the ±*y*-directions. The energy partition measured after the initial formation of the layer was $T_{\perp i}\sim\bar{Z}T_{\perp e} \geq 300$ eV (where $T_{\perp i,e}$ are the ion and electron temperatures measured perpendicular to E_{rec} and $\bar{Z}$ is the average ionization). These initial ion temperatures are much greater than can be accounted for by shock stagnation and viscous heating, and must draw from the magnetic energy of the inflows, channeled preferentially to the ions by an as-yet unidentified mechanism[34]. After the initial stages, $T_{\perp i}$ and $T_{\perp e}$ tend toward equilibrium in accordance with the decreasing energy-exchange time, as the density inside the layer increases due to the super-Alfvénic inflow. $T_{\perp i}$ and $T_{\perp e}$ are then regulated by the balance between the energy influx and the strong radiative cooling of the electrons[34].

In this work, we build on our past measurements to diagnose the distribution of energies in the out-of-plane direction. We show that the reconnection layer develops an anisotropic ion velocity distribution, with non-thermal tails parallel with the reconnection electric field, despite their thermal distribution in the perpendicular directions.

Enhanced Thomson scattering from electric field-aligned IAWs (834 words)

The main findings of our investigation come from our collective OTS diagnostic[36]. Our measurements probed ion-acoustic waves with wave-vectors orientated parallel (and anti-parallel) to $\boldsymbol{E_{rec}} = E_{rec}\hat{\boldsymbol{z}}$. We primarily employed the scattering geometry depicted in Fig. 1. The directions of the probe beam

and scattered light collection define the input and output wavevectors $\boldsymbol{K_{in}}$ and $\boldsymbol{K_{out}}$, which were at $\mp 30°$ to the reconnection plane respectively. Their symmetry about this plane set the resultant scattering wavevector $\boldsymbol{K} = \boldsymbol{K_{out}} - \boldsymbol{K_{in}}$, lying parallel to $\boldsymbol{E_{rec}}$ – thus Doppler shifts imprinted onto the scattered light (with $\Delta\omega = \boldsymbol{V} \cdot \boldsymbol{K}$) were sensitive to plasma waves along $\pm\hat{\boldsymbol{z}}$.

Discrete scattering volumes along the probe path were viewed simultaneously at 14 positions, distributed inside the layer and inflows on either side (Fig. 2a). This allowed OTS spectra to be sampled from each of these key regions. The spectral profiles shown in Fig. 2b-c were collected 80 ns after the formation of the reconnection layer, when previous measurements with $\boldsymbol{K}$ confined to the reconnection plane (perpendicular to $\boldsymbol{E_{rec}}$) have shown equilibrated electrons and ions[34].

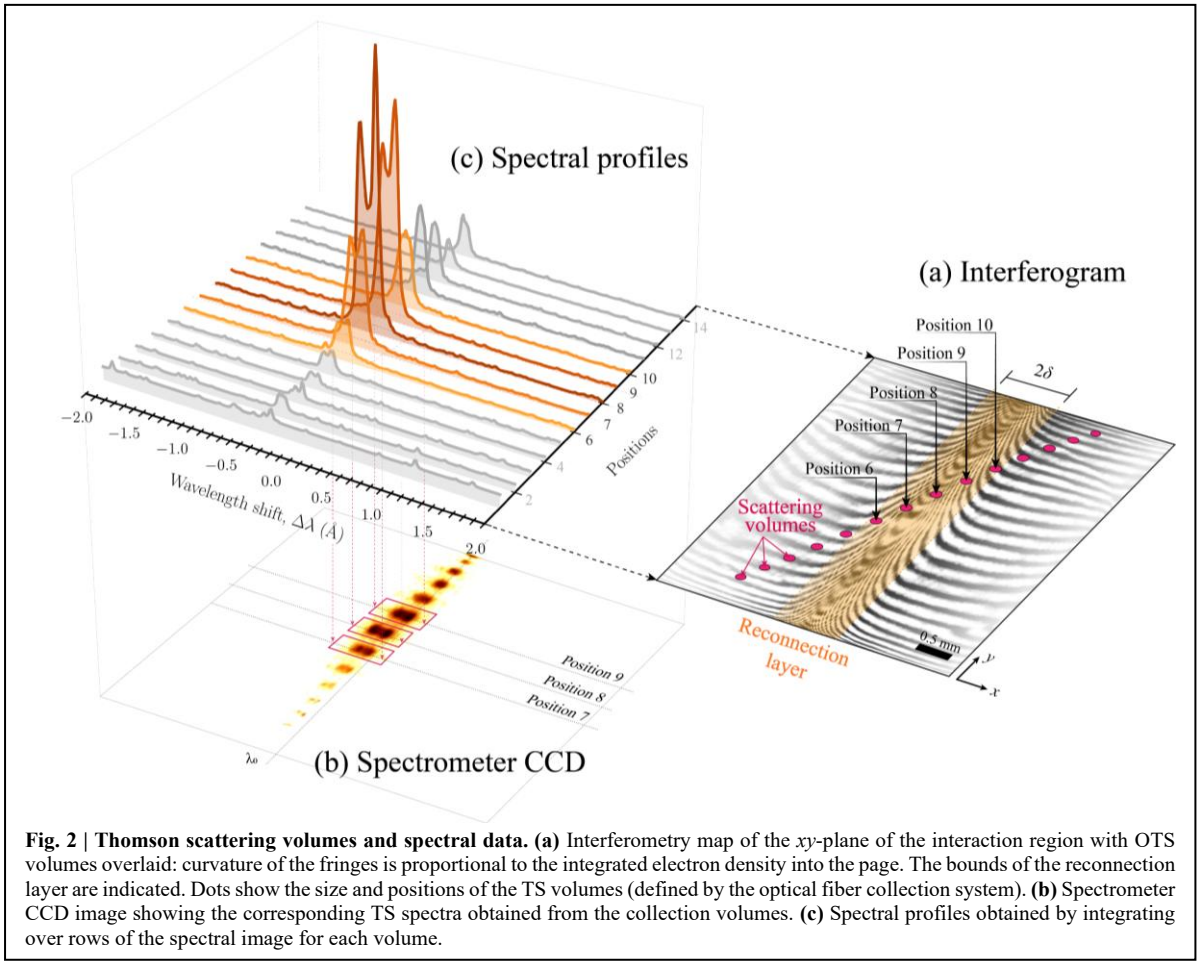


Fig. 2 | Thomson scattering volumes and spectral data. (a) Interferometry map of the *xy*-plane of the interaction region with OTS volumes overlaid: curvature of the fringes is proportional to the integrated electron density into the page. The bounds of the reconnection layer are indicated. Dots show the size and positions of the TS volumes (defined by the optical fiber collection system). **(b)** Spectrometer CCD image showing the corresponding TS spectra obtained from the collection volumes. **(c)** Spectral profiles obtained by integrating over rows of the spectral image for each volume.

The relative intensities of the spectral profiles in Fig. 2c have been corrected for the flat-field response of the spectrometer and optical coupling system. The scattered intensity from the layer is much greater than from the inflows, reaching a peak at the most central positions. The scattered power P_s incident at the detector in the frequency range $\omega_s \longrightarrow \omega_s + d\omega_s$ is expected to follow[29]

$$P_s(\omega_s)\mathrm{d}\Omega\mathrm{d}\omega_s \propto P_i n_e L S(\boldsymbol{K}, \omega)\mathrm{d}\Omega\mathrm{d}\omega_s, \qquad (1)$$

where P_i is the incident probe power, n_e the free electron density, L the length of the scattering volume along the probe direction, Ω the solid angle of the collection optics and S the spectral density function[29]

$$S(\boldsymbol{K},\omega) = \frac{2\pi}{K}\left|1-\frac{\chi_e}{\epsilon}\right|^2 f_e\left(\frac{\omega}{K}\right) + \frac{2\pi\bar{Z}}{K}\left|\frac{\chi_e}{\epsilon}\right|^2 f_i\left(\frac{\omega}{K}\right) \quad (2)$$

where f_e and f_i are the projections of the electron and ion distribution functions onto the direction of $\boldsymbol{K}$ and χ_e is the electron susceptibility. As the plasma is optically-thin and $P_s/P_i \ll 1$, the incident power can be assumed constant ($P_i = P_{i0}$) for each volume. L is also constant and n_e was independently constrained by laser interferometry (*see Methods*). Thus, $S(\boldsymbol{K},\omega)$ was used to fit the spectral profiles to identify the local plasma conditions.

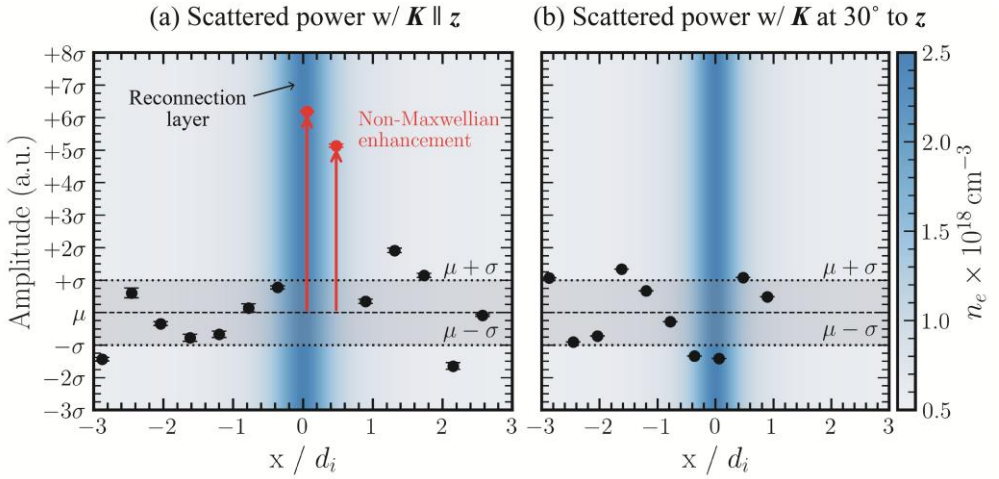


Fig. 3 | Enhancement of scattering from IAWs inside the reconnection layer aligned with the reconnection field. (a) Plot of OTS amplitude vs. position for OTS data obtained with $\boldsymbol{K}$ parallel to the z-axis (reconnection electric field). Electron density values from interferometry are over-plotted on the background color-map (blue). At positions outside the layer, the fitted amplitude is consistent with the expectation of a constant power probe beam, unattenuated as it passes through the optically-thin plasma. At highlighted positions (red arrows) inside the layer, the fitted laser amplitude for MB *S(K,ω)* fitting is a 6σ outlier with respect to the inflows. When physically constraining a constant amplitude (i.e. laser power), a non-MB ion distribution function must be used to generate *S(K,ω)* to obtain a good fit to the scattered power from these positions. **(b)** Spectra obtained simultaneously with $\boldsymbol{K}$ at 30° to the z-axis. The intensity profile is consistent with MB ion distribution functions at all positions – thus indicating that only scattering from waves closely aligned to the reconnection electric field is enhanced by non-MB effects.

For the collisional conditions in these experiments one would typically assume a Maxwell-Boltzmann (MB) distribution for f in Eq. 2, and this does indeed allow good fits to the shape of the OTS spectra from each volume. However, the amplitude of the two datapoints located most centrally in the layer (positions 8 and 9 in Fig. 2) can only be fit using a MB distribution in $S(\boldsymbol{K},\omega)$ if P_i is artificially increased at these positions to 3× the group average P_{i0} for the dataset. This is equivalent to an anomalous enhancement with 6σ significance in the local scattered power at the center of the layer (Fig. 3a) in comparison to the plasma in the inflows and edges of the layer, which are consistent with a common P_{i0} within errors as expected.

Significantly, this anomalous enhancement is not observed with a set of secondary OTS collection optics viewing the same positions simultaneously, with an associated scattering vector at 30° to $\hat{\boldsymbol{z}}$ (and hence sensitivity to IAWs waves in this off-vertical direction). The measured intensity from this scattering direction shows good agreement with a fixed P_{i0} when using MB-distribution fits (Fig. 3b). Further, we note that OTS data obtained in previous experiments[34] with $\boldsymbol{K}$ in the *xy*-plane also show good agreement between the measured intensity profile and that predicted with MB fitting.

We note that in our experiments, the intensity of the Thomson scattering probe beam is two orders of magnitude smaller than the threshold at which gains associated with stimulated Raman scattering and stimulated Brillouin scattering have recently been shown to modify the shape and intensity of OTS spectra[37]. Since our enhanced scattering is only observed in the out-of-plane direction, parallel to the current sheet of the reconnection layer, one could hypothesize it may be a signature of increased scattering from current-driven ion-acoustic turbulence (IAT). The electron drift velocity inferred from MB-distribution fits to the shape of the spectra (with unconstrained P_i) yield an electron drift velocity $\sim 2-4\times$ greater than the ion-acoustic speed c_S, which is a threshold for IAT in hydrogen plasmas[38]. However, the drift velocity threshold is much greater in multiply ionized plasmas due to strong Landau damping[39]. This is reflected in the shape of the OTS spectra in our experiment, which is not consistent with IAT. Enhanced scattering from IAWs has been observed in previous laboratory experiments[40,41]. This characteristically produces run-away scattering from only the IAW propagating in the direction of electron drift, with the counter-propagating wave limited to significantly lower, classical levels by Landau damping. Our data in contrast (Fig. 2), show an asymmetry in the amplitude of current-aligned IAWs in the layer, which is modest and consistent with both waves being regulated by Landau damping for an electron drift with the direction and magnitude imposed by $\boldsymbol{E_{rec}}$. We therefore conclude that the observed enhancement, which is strongly anisotropic in the direction of $\boldsymbol{E_{rec}}$, indicates the field must be modifying the underlying distribution function responsible for $S(\boldsymbol{K_z}, \omega)$.

Evidence of non-thermal ions pumped by the electric field (1355 words)

To constrain the ion distribution responsible for the anomalous scattering from the reconnection layer parallel to $\boldsymbol{E_{rec}}$, we relaxed the constraint of a MB-distribution for $f_i(V_z)$ in generating $S(\boldsymbol{K}, \omega)$ fits. We note that $S(\boldsymbol{K}, \omega)$ is not uniformly sensitive to f_i across velocity space – it is resonantly sensitive to df_i/dV in the region of c_S and vanishingly dependent beyond ~3-4c_S. This indicates an ion distribution with non-thermal characteristics in the regions $\pm 1-2c_S\hat{\boldsymbol{z}}$ could be responsible for the enhanced intensity. We note that for electrons a MB $f_e(V_z)$ was maintained for fitting, as the electron-electron collision times are very short in our experiments and the velocity space of any enhanced tails in the electron spectrum would be well-beyond the range of ω the OTS IAW feature is sensitive to.

To avoid converging to unphysical solutions for the ion distribution, we implemented a physically-motivated, parameterized model for f_i in our OTS fitting. Since non-thermal characteristics are most likely to arise in the distribution tail (as collisional frequency scales as $1/V^4$), we employed a model with MB bulk (with effective $T_{\|i}$, bulk velocity and electron drift velocity) and power law tails in $\pm V_z$ with start, cut-off and index parameters, as illustrated in Fig. 4a. Beyond the cut-off of the power-law, a MB tail was used for closure – thus allowing f_i to tend to a sum of MB distributions if this was more suitable than a power-law component.

The numerical speed and precision required to implement the Markov Chain Monte Carlo methods underlying this novel fitting approach were made possible by recent advancements in machine learning techniques (see *Methods* for details). Our routine converged on successful fits for the outlier datapoints inside the reconnection layer, which closely matched both the shape and intensity of the

spectra, as demonstrated in Fig. 4b for the central scattering volume from the layer. The lower amplitude MB fitting is overlaid for comparison to highlight its insufficient match to the scattered intensity.

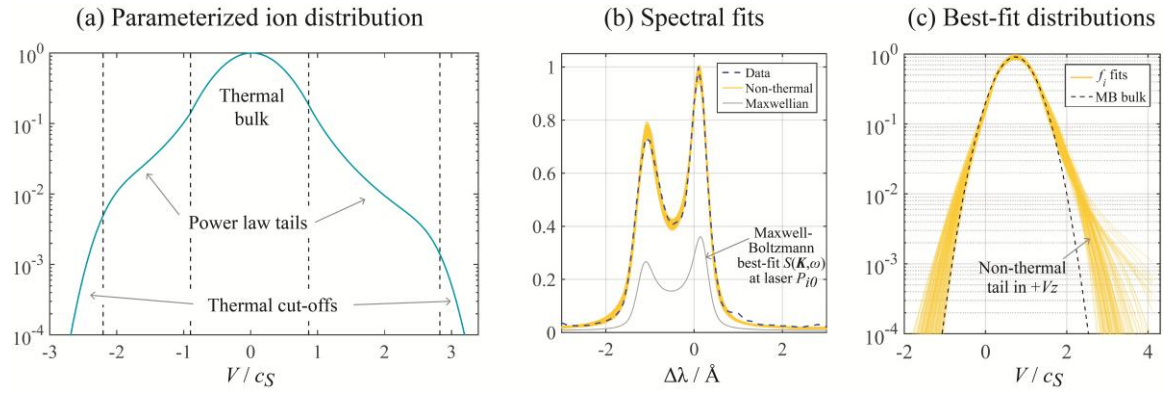


Fig. 4 | Non-thermal fitting of OTS spectra inside the reconnection layer. (a) Plot of the parameterized ion distribution function used for the spectral fitting routine. The shape of the distribution function consisted of a MB bulk with temperature, bulk velocity and drift velocity parameters, and positive and negative velocity power law tails, with indices, starting velocity and cut-off velocity parameters. **(b)** Comparison of MB and non-MB fits to the OTS spectrum with $\boldsymbol{K}_z$ from the center of the layer. **(c)** Ion distribution functions used to generate $S(\boldsymbol{K},\omega)$ for the fitting shown in (b). Overlaid (dashed line) is the extrapolated shape of the MB bulk. The velocity axis is normalized to the ion acoustic speed.

The ion distributions from the 100 best-fits to the OTS spectrum in Fig. 4b are shown in Fig. 4c. They reveal a highly asymmetric distribution, with a thermal bulk at $T_{\parallel i} = 68 \pm 3$ eV and significantly amplified non-thermal tails in both $\pm V_z$. The $+V_z$ tail is most prominent, consistent with the acceleration of positively charged ions experiencing $\boldsymbol{E_{rec}}$, extending to over $3c_S (= 7V_{Ti})$ with respect to the bulk. We note the fitted $T_e = 27 \pm 1$ eV is consistent with previous measurements in the reconnection plane.

The departure of the ion distribution from thermal equilibrium is a remarkable result, given the considerable collisionality of the plasma in the reconnection layer. Using the measured plasma parameters we calculate E_{rec} in our system: using either the inflow $V_x \times B_y$ or ηJ_z inside the layer (where J_z is the current density of a Harris sheet fit to the upstream magnetic field, see *Methods*). These give a consistent value of 200 kV/m. In this field an acceleration length of $\Delta z = 1$ mm is required to reach the observed tail energies. This is well within the out-of-plane system-size of the layer (20 mm), but is much greater than the mean free path for ion-ion collisions: ranging from 10^{-4} mm in the bulk of the distribution to 0.3 mm in the tail. At these conditions the ions travelling at 3-4c_S would be expected to experience a collisional loss rate $dE/dt^{i\backslash i}$ approximately 5-10x greater than the acceleration power $\bar{Z}eE_{rec}V_z$, raising the question of how this non-thermal signature can be sustained in the presence of such a dominant loss channel.

To shed light on this unintuitive result we performed fully-kinetic simulations of the system to investigate the underlying ion dynamics. Our simulations employed the state-of-the-art, collisional particle-in-cell code OSIRIS 4.0[42], with experimentally matched ion collisionality $\lambda_{ii}/d_i = 10^{-4}$, reconnection layer aspect ratio $L/d_i = 100$ and inflow Mach number $V_x/V_A = 2$ (see *Methods* for

details). The simulations spatially modelled the 2D reconnection plane, with 3D velocity and electromagnetic field components and collisions between all species in each of these dimensions.

The results of the simulations are shown in Fig. 5. The current density in the reconnection plane (Fig. 5a) demonstrates the formation of the layer and the pile-up of flux at its boundaries due to the super-Alfvénic inflows. The ion V_z distribution in the box centered on the layer with bounds $|x| < 2.5d_i$ and $|y| < 10d_i$ is plotted in Fig. 5b. This exhibits an asymmetric tail starting around $+2c_S$, and qualitatively replicates the result from the experimental TS spectra. Meanwhile, the V_x and V_y components in the simulated layer possess ± symmetry, and thermal distributions as expected.

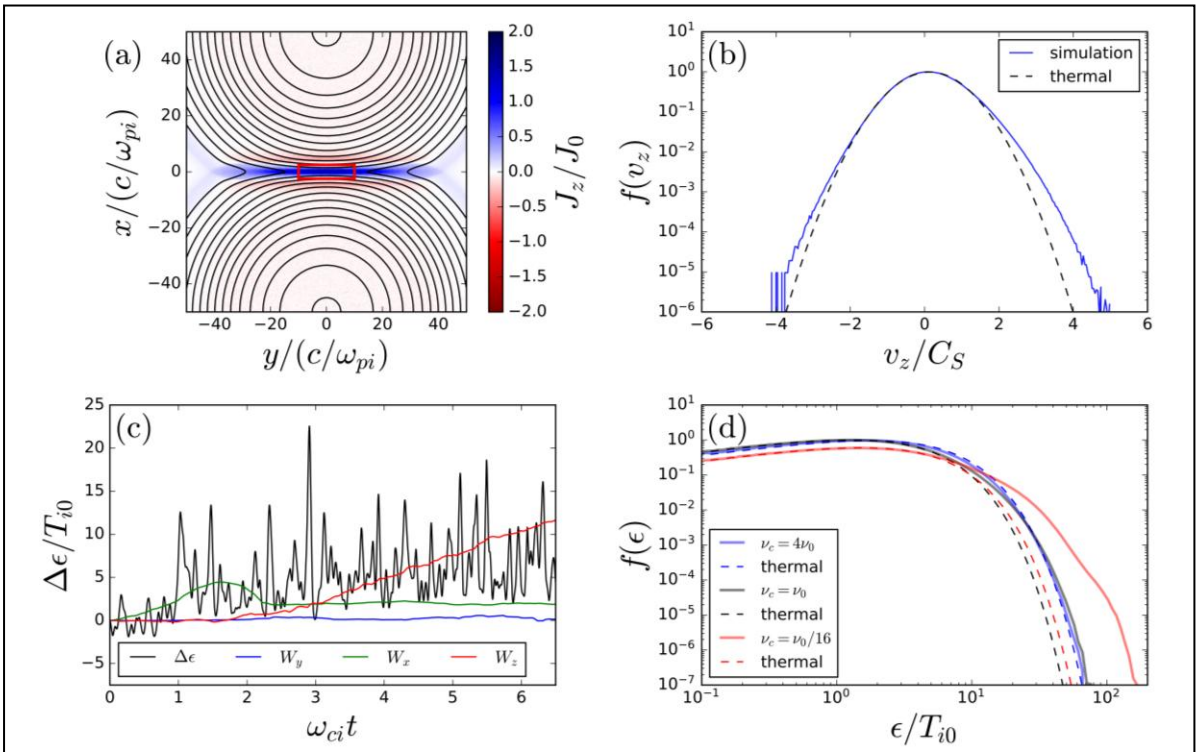


Fig. 5 | Collisional PIC simulations with matched ion dynamics. (a) Map of the out-of-plane current density of the reconnection plane, including contributions from electrons and ions, with overlaid magnetic field lines. Current density is normalized to the characteristic value $J_0 = B_0/\mu_0 d_i$, where B_0 is the initial characteristic inflow magnetic field strength. The red box shows the selection region for the distribution function shown in b (taken at the same time snapshot). **(b)** Out-of-plane velocity distribution of ions in the red box, normalized to the ion acoustic speed. The simulation reveals the development of an asymmetric, non-thermal ion tail due to acceleration in the direction of $\boldsymbol{E_{rec}}$ near the X-point. A thermal fit to the bulk of the distribution is shown for comparison. **(c)** Typical ion energization in the layer, showing: the change in total ion energy (black) relative to the initial inflow energy, and cumulative work done by the three components of the electric field. The ion energy is expressed in units of the initial ion temperature. **(d)** Out-of-plane ion energy distributions for: the experimentally-matched collision-rate (ν_0), and with increased and decreased collision rates. The bulk of the distributions have been fit with MB-distributions to illustrate convergence/departure from thermal equilibrium in the tails.

To investigate the ion acceleration mechanism in the simulation, we tracked the trajectory and energy history of several sample populations (each 1024 particles) inside the reconnection layer. We looked separately at ions with different initial V_z: from those initially in the distribution bulk, out to several multiples of c_S. Fig. 5c shows a typical energy history for an ion with initial $V_z \sim 2c_S$. In all cases, the ions remained confined to the layer in *x*, with only short-lived excitations in V_z above the baseline of the distribution (with typical duration $\omega_{ci}t \sim 0.1$, equivalent to 1 ns in the experiments and 10^3 simulation timesteps). This suggests the non-thermal tail does not arise from a small population of ions making large runaway gains, but rather a systematic, statistical perturbation to the V_z-distribution

is acquired through the time-averaged energization of the ions, set by the competition between the asymmetric $\boldsymbol{E_{rec}}$ drive near the X-point and the V^{-3}-dependent collisional drag.

Our simulations highlight the importance of collisions in moderating the prominence of the non-thermal tail. Additional simulations with fully-suppressed ion-ion collisions showed a significantly distorted tail, demonstrating that ion-electron collisions alone are insufficient to reproduce the experiments. Scans of the ion-ion collision rate indicate our experiments lie in a very interesting region of the parameter space, close to the threshold for non-thermal effects. At the experimentally-matched ion-ion collision rate ν_0, the energy in the non-thermal component of the distribution (fitting $f(\epsilon)$ from $0 \rightarrow f_{max}$) was $E_{non-thermal}/E_{total} = 8\%$. On increasing collisionality to $4\nu_0$, T_i of the bulk increased by 40%, while the non-thermal residual of the tail was effectively suppressed (Fig. 5d). Conversely, at $\nu_0/16$ a more prominent tail was produced with $E_{non-thermal}/E_{total} = 22\%$. This behavior motivates the design of future experiments at lower collisionality within the $\lambda_{ii} \ll d_i$regime. Such conditions could be achieved in pulsed-power experiments through the use of higher atomic number elements, which produce comparable mass density flows, with a greater ion kinetic energy and stopping distance[43].

These results have significant implications for magnetic reconnection as a non-thermal particle accelerator. While non-thermal acceleration in reconnection has been studied across a wide range of regimes[13,14,18], the plasmas are typically assumed to be near-collisionless. Where collisional effects have been considered, studies primarily addressed their role in setting the structure of the current layer[44], with frequent collisions expected to preclude significant departures from thermal equilibrium. The presence of a detectable non-thermal signature in our experiments and simulations at non-relativistic conditions, modest Lundquist number and high collisionality therefore demonstrates non-thermal ion acceleration could be a widespread feature in flow-dominated reconnection systems. These results will motivate improved models to capture the onset and properties of nonthermal ion acceleration in collisional reconnection regimes.

Our findings highlight that particle acceleration can occur in driven ($M_A \geq 1$) collisional reconnection, relevant to both laboratory and astrophysical plasmas. One significant context could be in controlled fusion plasmas, where reconnection of applied or self-generated magnetic fields could lead to the presence of non-thermal tails, impacting heat transport of ignition regions. Non-thermal ion tails driven by the reconnection electric field against collisional drag were identified in the Mega-Ampere Spherical Tokamak (MAST), where a suprathermal ion population was observed following internal reconnection events in weakly collisional regimes[45]. Our results suggest that ion acceleration could persist even at higher collisionalities.

Finally, the solar chromosphere presents a compelling context for future investigation, where reconnection is ubiquitous[46] and the mechanisms driving heating remain an open question[47]. Chromospheric plasmas span $\lambda_{ii}/d_i \sim 10^{-2} - 10^{0}$ and posses $M_A \geq 1$ inflows driven by convective motions[48], where our results show the non-thermal ion tail becomes more prominent as collisionality

259 decreases towards this range. We note however that chromospheric plasmas are partially ionized,
260 requiring a dedicated analysis beyond the scope of this work.

METHODS (1585/3000)

Magnetic reconnection with ablating wire arrays (217 words)

The dual wire array setup used in these experiments is shown schematically in Fig. 1. The cylindrical arrays each consisted of 16, 30 μm-diameter aluminum wires, equally spaced around a 5 mm-diameter central conductor. The arrays were 16 mm in diameter, 20 mm in height and separated by an axis-to-axis distance of 27 mm. The current applied (in parallel) to the wire arrays by the MAGPIE generator can be approximated by the form $I(t) = I_0 \sin^2(\pi t/500\ \mathrm{ns})$, where $I_0 \simeq 1$ MA. It passes up the wires and down the central conductor. The counter-streaming plasma flows produced by the arrays are formed by the resistive ablation of the wires. The ablation streams from the individual wires merge to form a combined flow carrying an embedded magnetic field[31].

The magnetic reconnection layer formed by the collision of the flows has an approximately constant half-width thickness of $\delta = d_i = 0.3$ mm. The properties of the inflows and the reconnection layer have been extensively characterized in previous works[33,34] using a suite of laser probing diagnostics[35,36]. Table I summarizes their key parameters at the corresponding time in the reconnection layer development discussed in this paper (250ns after current start in the wire arrays, 80ns after reconnection layer formation). Temperatures with a subscript $\perp$ indicate they were measured in the reconnection plane (orthogonal to the reconnection electric field).

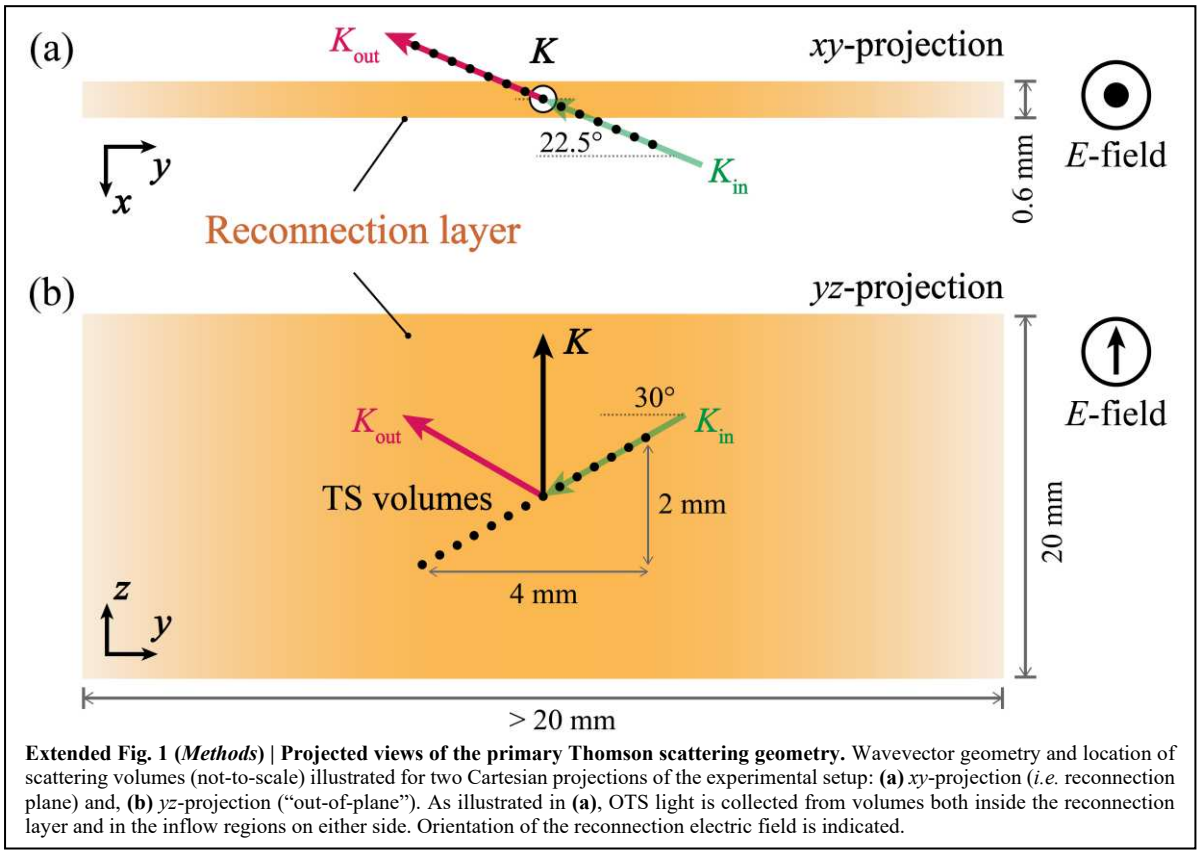
Parameter	Symbol	Inflow	Reconnection layer
In-plane electron temperature (eV)	$T_{\perp e}$	15	30
In-plane ion temperature (eV)	$T_{\perp i}$	20	30
Ionization	$\bar{Z}$	3.5	6
Electron density (cm^{-3})	n_e	5×10^{17}	2.5×10^{18}
Magnetic field (T)	B_y	4	-
Inflow (outflow) velocity (km/s)	V_{in} (V_{out})	50	(100)
Alfvén speed (km/s)	V_A	35	-
Ion sound speed (km/s)	c_S	20	30
Ion thermal speed (km/s)	V_{Ti}	8	10
Reconnection electric field (kV/m)	$E_{rec} = V_x \times B_y$	200	-
	$E_{rec} = \eta J_z$	-	200
Inflow Alfvénic Mach number	M_A	1.4	-
Thermal Beta	$\beta = 2\mu_0 n k_B T/B^2$	0.4	-
Lundquist number	S		20
Electron Hall parameter	$\Omega_{ce}\tau_{ei}$	1	-
Ion Hall parameter	$\Omega_{ci}\tau_{ii}$	0.001	-
Layer half-thickness (mm)	δ	-	0.3
Ion-ion mean free path (mm)	λ_{ii}	10^{-4}	10^{-5}
Ion skin depth (mm)	$d_i = c/\omega_{pi}$	0.9	0.3
Radiative cooling time (ns)	τ_{rad}	20	5
Ion-electron thermal equilibration time (ns)	τ_{ei}^E	50	20

Table I: Past measurements of plasma parameters in the reconnection plane in the inflows and reconnection layer at the time of the results discussed in this paper[33,34].

Optical Thomson scattering probe (454 words)

The spatially resolved OTS diagnostic used for these experiments is described in detail in Ref. [36]. It probed the spectra of ion-acoustic waves (IAWs) in the collective regime with $\alpha = 1/\lambda_D K \sim 2 - 3$[29]. The Dopper shifts of the IAW spectra with respect to the laser probe ω are sensitive to plasma motion in the direction of the scattering vector ($\Delta\omega = \boldsymbol{V} \cdot \boldsymbol{K}$).

The primary OTS geometry used in the experiment is shown in Fig. 1. Extended figs. 1a and 1b show the projections of this geometry onto the planes *xy* and *yz* respectively. The probe crossed the layer at −22.5° as projected onto *xy* (close to the layer's mid-position in *y* and *z*) and was at −30° to *xy*. Scattered light was observed at +30° to *xy*, in the plane defined by $\boldsymbol{K_{in}}$ and $\hat{\boldsymbol{z}}$. The discrete scattering volumes along the path of $\boldsymbol{K_{in}}$ are indicated.



Extended Fig. 1 (*Methods*) | Projected views of the primary Thomson scattering geometry. Wavevector geometry and location of scattering volumes (not-to-scale) illustrated for two Cartesian projections of the experimental setup: **(a)** *xy*-projection (*i.e.* reconnection plane) and, **(b)** *yz*-projection ("out-of-plane"). As illustrated in **(a)**, OTS light is collected from volumes both inside the reconnection layer and in the inflow regions on either side. Orientation of the reconnection electric field is indicated.

In addition to the primary scattering geometry, an additional (secondary) geometry was used. This utilized the same laser probe, and hence shares the same input wavevector $\boldsymbol{K_{in}}$. Scattering was viewed simultaneously from the same volumes, from a purely vertical scattering angle (such that the secondary output vector $\boldsymbol{K_{out,2}}$ pointed in the z-direction). The scattering vector $\boldsymbol{K_2} = K_2[-\sin(30°)\sin(22.5°)\hat{\boldsymbol{x}}, -\sin(30°)\cos(22.5°)\hat{\boldsymbol{y}}, \cos(30°)\hat{\boldsymbol{z}}] = K_2[-0.19\hat{\boldsymbol{x}}, -0.46\hat{\boldsymbol{y}}, 0.86\hat{\boldsymbol{z}}]$ associated with this secondary collection system was therefore offset by an angle of 30° to the *z*-axis and hence $\boldsymbol{E_{rec}}$.

The OTS diagnostic used a focused laser probe (Nd:YAG 2ω, λ=532 nm, 7 ns FWHM, 2 J) with a beam waist of $\sim 200\ \mu$m throughout the range of interest of the plasma. At both the primary and secondary viewing angles the scattered light was collected using a single lens system to image the path of the

laser beam onto the input of a fiber-optic bundle. The imaging system (*f*=20cm, Ø2", NA=0.06) gave a $\times 0.8$ magnification. The bundles consisted of 14 individual, 100 μm-diameter fibers, giving collection volumes 125 μm in diameter, spaced by 0.3 mm along the beam path. The scattering volumes were approximately centred on the layer in both the *y* and *z* axes, spanning ranges of Δ*y* = 4 mm and Δ*z* = 2 mm, which were much smaller the overall length and height of the layer (*L*, *h* ≳ 20 mm).

The outputs from the fiber-optic bundles were recorded using an imaging spectrometer (ANDOR SR-500i-A, with gated ANDOR iStar ICCD camera). The spectral resolution of 0.25 Å was set by the combination of the 50 μm spectrometer slit width and 2400 lines/mm grating, and the temporal resolution was set by the 4 ns gate time of the camera. The instrument response of the spectrometer in spectral space was found by recording the spectrum of the (monochromatic) laser probe for each of the individual collection optical fibres on the spatial axis of the spectrometer CCD.

Local electron density constrained by laser interferometry (182 words)

A Mach-Zehnder laser interferometer was used to measure the (line-integrated) electron density of the plasma[35]. Interferograms of the xy-plane (Fig. 2a) were obtained by probing along the *z*-direction, using the 2nd harmonic (532 nm) of a pulsed Nd:YAG laser (EKSPLA SL321P, 0.3 ns, 500 mJ). The interferograms were processed to produce maps of electron line density ($\int n_e \mathrm{d}z$) using the analysis procedure described in Ref. [35]. These were converted to electron density (n_e) by dividing by the height of the arrays (Δz=20 mm), owing to the uniformity of the setup in the *z*-direction. The measurements of electron density were used to constrain the fitting of the OTS spectra. The coordinates of the scattering volumes were identified within the *xy*-plane of the interferometry images to a precision of ≤200 μm, using the procedure described in Ref. [35], ensuring the correct electron density values were matched with the OTS volumes. We note the IAW component of $S(\omega,\boldsymbol{K})$ is weakly dependent on n_e in the range of densities encountered in these experiments, so any errors in n_e using this technique do not perceivably impact the fitting.

Collisional PIC simulations with matched ion dynamics (248 words)

2D-3V (two spatial dimensions and three velocity and field components) collisional PIC simulations of the *xy*-plane of the reconnection region were performed with OSIRIS 4.0[42], using the initial configuration described in Ref. 15. The simulations employed experimentally matched parameters for the ion dynamics, including: collisionality $\lambda_{ii}/d_i = 10^{-4}$, reconnection layer aspect ratio $L/d_i = 100$, inflow Mach number $V_x/V_A \sim 2$ and ion mass $m_i = 27m_p$. Due to limited computational resources a reduced mass ratio of $m_i/m_e = 600$ was used (with average ionization $\hat{Z}$ matching the experiments). To preserve ion and electron transport properties in the presence of this reduced mass ratio, the collisional scaling method described in Ref. [49] was applied. We note that the radiative properties of the plasma were not captured in the simulations, so the absolute values of temperature were not expected to match the experiments due to the absence of this cooling channel.

The domain size of the simulations was $x \times y = 200d_i \times 100d_i$, with 20 cells per d_i. The simulations used a temporal resolution of $\omega_{pe}dt = 0.35$ and 256 particles per-cell per-species. Additional

convergence studies were performed with an increased temporal resolution of $\omega_{pe}dt = 0.35/16$ to verify the robustness of the results and rule out numerical artefacts. Scans to test the sensitivity of the out-of-plane ion velocity distribution in the simulations to the ion-ion collision rate were performed by applying a multiplicative factor to the effective Coulomb logarithm, which the collisional rates are proportional to. The range $\nu_0/16$ to $16\nu_0$ was explored. For particle tracking within the simulations, sets of 1024 simulations particles were used.

Non-thermal IAW OTS fitting (484 words)

Spectral fitting of the anomalous intensity IAW OTS spectra from locations 8 and 9 in the reconnection layer (Fig. 2a) was performed using the non-relativistic, collective spectral density function (Eq. 2) with non-MB f_i. The amplitude of the fits (Eq. 1) was set using the measured electron density and the amplitude distribution fit to the fibers which sampled outside the layer, i.e. those well-fit by MB ion distributions. The functional form of f_i used to fit the data was composed of a thermal MB bulk (with effective temperature T_i, bulk velocity V_i and relative electron drift velocity V_{ei}) and power-law tails in $\pm V_z$ (with V_{start}, width and index parameters). Termination at the cut-off of the power-law was provided by return to MB (exponential) decay. A MB f_e was applied, which yielded fits to T_e consistent with that measured in the reconnection plane at comparable times in the experiment. The electron temperature and density were also used to find the ionization level using tabulated $\bar{Z}$ values from FLYCHK[50]. The drift velocity V_{ei} of electrons relative to the ion bulk used an upper-limit set by the maximum current density that could sustain the largest magnetic field gradient consistent with Faraday rotation measurements of the magnetic field profile across the layer[34].

The full model for the measured IAW signal includes a flat background, a model IAW spectrum and convolution with a measured wavelength-space instrumental response. The model IAW spectrum is calculated from a proposed ion distribution from Eq. 2. A novel computer program to calculate this spectrum is written in Python JAX for two reasons. Firstly, the just-in-time compilation allows for performant code which can be run on accelerators. And secondly, it allows for automatic differentiation (AD) which is very valuable in the calculation of the ion susceptibility χ_i, as this involves a calculation of the plasma dispersion function. This involves an integral of the form:

$$Z_i'(u) = \int dv \frac{df_i/dv}{v-u}$$

We therefore need the derivative of our proposed ion distribution to high accuracy; AD can do this to machine precision. The principal value integral is handled using the method of Keller and Wróbel, Legendre-Gauss adaptive quadrature ensures high accuracy of the resulting numerical integrals. Gradients through the adaptive quadrature can be calculated using Leibniz integral rule – this capability is necessary to utilize gradient descent fitting methods. The full calculation of IAW model spectrum from a proposed non-MB distribution takes of order 100 ms on 8 CPU cores. This is suitably efficient to allow Markov Chain Monte Carlo (MCMC) methods to be used to find the best fit to data and quantify uncertainties. In this work, we used the emcee package to perform the MCMC to minimize the least-squares error in addition to a regularizing prior that the gradient df_i/dv transition

between power-law tails and MB bulk should be smooth. Where separate measurements are available, e.g. interferometry and Faraday rotation for n_e and V_{ei} respectively, these are included into the priors.

FUNDING STATEMENTS

L.G.S. and the experimental work were supported by NNSA under DOE Cooperative Agreements DE-NA0004148, DE-NA0003764, DE-F03-02NA00057 and DE-SC-0001063. J.W.D.H. was supported by the DTRA under Award No. HDTRA1-20-1-0001. F.F was supported by the European Research Council (ERC-2021-CoG Grant XPACE No.~101045172). A.J.C. was supported by Schmidt Sciences, LLC, the International Atomic Energy Agency AI for Fusion CRP and the Imperial College Research Fellowship program. S.M. was supported by AFOSR under FA8655-23-1-7062.

AUTHOR CONTRIBUTION STATEMENTS

L.G.S., J.D.H., S.V.L. and J.W.D.H. conceived the experiments. L.G.S., J.W.D.H., J.D.H., V.V.V., S.M. and S.V.L. performed the experiments. A.J.C., C.B., L.G.S., J.W.D.H. and S.V.L. analyzed experimental data. A.J.C. and C.B. developed computational techniques for the analysis procedure. S.R.T. performed computational simulations with input from F.F. L.G.S., J.W.D.H., F.F., S.R.T., V.V.V., C.B., W.R. and S.V.L. interpreted the results. L.G.S., S.M. and S.R.T. produced the figures. L.G.S. wrote the manuscript with contributions from all authors. All authors discussed the results, commented on the manuscript and approved the final version.

References (50 / 50 reference limit)

1. Yamada, M. *Magnetic Reconnection*. (Princeton University Press, Princeton, N.J., 2022). doi:10.1515/9780691232980.
2. Igochine, V. Magnetic reconnection during sawteeth crashes. *Phys. Plasmas* **30**, (2023).
3. Zocco, A., Helander, P. & Weitzner, H. Magnetic reconnection in 3D fusion devices: non-linear reduced equations and linear current-driven instabilities. *Plasma Phys. Control. Fusion* **63**, 025001 (2021).
4. Joglekar, A. S., Thomas, A. G. R., Fox, W. & Bhattacharjee, A. Magnetic Reconnection in Plasma under Inertial Confinement Fusion Conditions Driven by Heat Flux Effects in Ohm's Law. *Phys. Rev. Lett.* **112**, 105004 (2014).
5. Case, N. A., Grocott, A., Milan, S. E., Nagai, T. & Reistad, J. P. An analysis of magnetic reconnection events and their associated auroral enhancements. *J. Geophys. Res. Sp. Phys.* **122**, 2922–2935 (2017).
6. Chitta, L. P. *et al.* A magnetic avalanche as the central engine powering a solar flare. *Astron. Astrophys.* **705**, A113 (2026).
7. Jia, H. *et al.* Millimeter observational signatures of flares in magnetically arrested black hole accretion models. *Mon. Not. R. Astron. Soc.* **526**, 2924–2941 (2023).
8. Ripperda, B. *et al.* Black Hole Flares: Ejection of Accreted Magnetic Flux through 3D Plasmoid-mediated Reconnection. *Astrophys. J. Lett.* **924**, L32 (2022).
9. Drake, J. F., Opher, M., Swisdak, M. & Chamoun, J. N. A MAGNETIC RECONNECTION MECHANISM FOR THE GENERATION OF ANOMALOUS COSMIC RAYS. *Astrophys. J.* **709**, 963–974 (2010).
10. Giannios, D. UHECRs from magnetic reconnection in relativistic jets. *Mon. Not. R. Astron. Soc. Lett.* **408**, L46–L50 (2010).
11. Shukla, A. & Mannheim, K. Gamma-ray flares from relativistic magnetic reconnection in the jet of the quasar 3C 279. *Nat. Commun.* **11**, 4176 (2020).
12. Rajhans, A. *et al.* Energy Partitioning Between Thermal and Non-Thermal Electrons and Ions in Magnetotail Reconnection. *Geophys. Res. Lett.* **52**, (2025).
13. Oka, M. *et al.* Particle Acceleration by Magnetic Reconnection in Geospace. *Space Sci. Rev.* **219**, (2023).
14. Guo, F., Liu, Y.-H., Zenitani, S. & Hoshino, M. Magnetic Reconnection and Associated Particle Acceleration in High-energy Astrophysics. http://arxiv.org/abs/2309.13382 (2023).
15. Totorica, S. R., Abel, T. & Fiuza, F. Nonthermal Electron Energization from Magnetic Reconnection in Laser-Driven Plasmas. *Phys. Rev. Lett.* **116**, 095003 (2016).
16. Hoshino, M. Efficiency of nonthermal particle acceleration in magnetic reconnection. *Phys. Plasmas* **29**, (2022).
17. Lu, S. *et al.* Turbulence and Particle Acceleration in Collisionless Magnetic Reconnection: Effects of Temperature Inhomogeneity across Pre-reconnection Current Sheet. *Astrophys. J.* **878**, 109 (2019).
18. Guo, F. *et al.* Recent progress on particle acceleration and reconnection physics during

magnetic reconnection in the magnetically-dominated relativistic regime. *Phys. Plasmas* **27**, (2020).

19. Uzdensky, D. A. Relativistic non-thermal particle acceleration in two-dimensional collisionless magnetic reconnection. *J. Plasma Phys.* **88**, 905880114 (2022).

20. Li, X., Guo, F., Liu, Y.-H. & Li, H. A Model for Nonthermal Particle Acceleration in Relativistic Magnetic Reconnection. *Astrophys. J. Lett.* **954**, L37 (2023).

21. Medina-Torrejón, T. E., de Gouveia Dal Pino, E. M. & Kowal, G. Particle Acceleration by Magnetic Reconnection in Relativistic Jets: The Transition from Small to Large Scales. *Astrophys. J.* **952**, 168 (2023).

22. Marsch, E. Helios: Evolution of Distribution Functions 0.3–1 AU. *Space Sci. Rev.* **172**, 23–39 (2012).

23. Gosling, J. T. *et al.* Interplanetary ions during an energetic storm particle event: The distribution function from solar wind thermal energies to 1.6 MeV. *J. Geophys. Res. Sp. Phys.* **86**, 547–554 (1981).

24. Phan, T. D. *et al.* Parker Solar Probe Observations of Solar Wind Energetic Proton Beams Produced by Magnetic Reconnection in the Near-Sun Heliospheric Current Sheet. *Geophys. Res. Lett.* **49**, (2022).

25. Graham, D. B. *et al.* Non-Maxwellianity of Electron Distributions Near Earth's Magnetopause. *J. Geophys. Res. Sp. Phys.* **126**, (2021).

26. Stansby, D., Horbury, T. S. & Matteini, L. Diagnosing solar wind origins using in situ measurements in the inner heliosphere. *Mon. Not. R. Astron. Soc.* **482**, 1706–1714 (2019).

27. Shi, P. *et al.* Laboratory Observations of Electron Heating and Non-Maxwellian Distributions at the Kinetic Scale during Electron-Only Magnetic Reconnection. *Phys. Rev. Lett.* **128**, 025002 (2022).

28. Chien, A. *et al.* Non-thermal electron acceleration from magnetically driven reconnection in a laboratory plasma. *Nat. Phys.* **19**, 254–262 (2023).

29. Froula, D. H., Glenzer, S. H., Luhmann, N. C. J. & Sheffield, J. *Plasma Scattering of Electromagnetic Radiation*. (Elsevier, 2011). doi:10.1007/s13398-014-0173-7.2.

30. Mitchell, I. H. *et al.* A high impedance mega-ampere generator for fiber z -pinch experiments. *Rev. Sci. Instrum.* **67**, 1533–1541 (1996).

31. Suttle, L. G. *et al.* Interactions of magnetized plasma flows in pulsed-power driven experiments. *Plasma Phys. Control. Fusion* **62**, 014020 (2020).

32. Hare, J. D. *et al.* An experimental platform for pulsed-power driven magnetic reconnection. *Phys. Plasmas* **25**, 055703 (2018).

33. Suttle, L. G. *et al.* Structure of a Magnetic Flux Annihilation Layer Formed by the Collision of Supersonic, Magnetized Plasma Flows. *Phys. Rev. Lett.* **116**, 225001 (2016).

34. Suttle, L. G. *et al.* Ion heating and magnetic flux pile-up in a magnetic reconnection experiment with super-Alfvénic plasma inflows. *Phys. Plasmas* **25**, 042108 (2018).

35. Swadling, G. F. *et al.* Diagnosing collisions of magnetized, high energy density plasma flows using a combination of collective Thomson scattering, Faraday rotation, and interferometry (invited)a). *Rev. Sci. Instrum.* **85**, 11E502 (2014).

36. Suttle, L. G. *et al.* Collective optical Thomson scattering in pulsed-power driven high energy density physics experiments (invited). *Rev. Sci. Instrum.* **92**, 033542 (2021).

37. Turnbull, D., Milder, A. L., Follett, R. K., Katz, J. & Froula, D. H. Thomson Scattering with Gain. *Phys. Rev. Lett.* **136**, 135101 (2026).

38. Bychenkov, V. Y., Silin, V. P. & Uryupin, S. A. Ion-acoustic turbulence and anomalous transport. *Phys. Rep.* **164**, 119–215 (1988).

39. Ryutov, D. D., Derzon, M. S. & Matzen, M. K. The physics of fast Z pinches. *Rev. Mod. Phys.* **72**, 167–223 (2000).

40. Daughney, C. C., Holmes, L. S. & Paul, J. W. M. Measurement of Spectrum of Turbulence Within a Collisionless Shock by Collective Scattering of Light. *Phys. Rev. Lett.* **25**, 497–499 (1970).

41. Milder, A. L. *et al.* Direct Measurement of the Return Current Instability in a Laser-Produced Plasma. *Phys. Rev. Lett.* **129**, 115002 (2022).

42. Fonseca, R. A. *et al.* OSIRIS: A Three-Dimensional, Fully Relativistic Particle in Cell Code for Modeling Plasma Based Accelerators. in *Lecture Notes in Computer Science (including subseries Lecture Notes in Artificial Intelligence and Lecture Notes in Bioinformatics)* vol. 2331 LNCS 342–351 (2002).

43. Harvey-Thompson, A. J. *et al.* Optical Thomson Scattering Measurements of Plasma Parameters in the Ablation Stage of Wire Array Z Pinches. *Phys. Rev. Lett.* **108**, 145002 (2012).

44. Ji, H. & Daughton, W. Phase diagram for magnetic reconnection in heliophysical, astrophysical, and laboratory plasmas. *Phys. Plasmas* **18**, 111207 (2011).

45. Helander, P. *et al.* Ion Acceleration during Reconnection in MAST. *Phys. Rev. Lett.* **89**, 235002 (2002).

46. Shibata, K. *et al.* Chromospheric Anemone Jets as Evidence of Ubiquitous Reconnection. *Science (80-.).* **318**, 1591–1594 (2007).

47. Carlsson, M., De Pontieu, B. & Hansteen, V. H. New View of the Solar Chromosphere. *Annu. Rev. Astron. Astrophys.* **57**, 189–226 (2019).

48. Ni, L., Kliem, B., Lin, J. & Wu, N. FAST MAGNETIC RECONNECTION IN THE SOLAR CHROMOSPHERE MEDIATED BY THE PLASMOID INSTABILITY. *Astrophys. J.* **799**, 79 (2015).

49. Totorica, S. R., Lezhnin, K. V. & Fox, W. Particle collisionality in scaled kinetic plasma simulations. *Comput. Phys. Commun.* **319**, 109899 (2026).

50. H.-K. Chung, M.H. Chen, W.L. Morgan, Yu. Ralchenko, R. W. L. FLYCHK: Generalized population kinetics and spectral model for rapid spectroscopic analysis for all elements. *High Energy Density Phys. v.1, p.3* https://doi.org/https://dx.doi.org/10.18434/T4WS3G (2005) doi:https://dx.doi.org/10.18434/T4WS3G.